

Topological Hall effect in monolayer 1T'-MoS₂

Mohammad Mortezaei Nobahari^{ib} and Mahmood Rezaei Roknabadi^{ib}

Department of Physics, Ferdowsi University of Mashhad, Iran

(Dated: January 22, 2025)

1T' phase of the monolayer transition metal dichalcogenides has recently attracted attention for its potential in nanoelectronic applications. This study proves the topological behavior of 1T'-MoS₂ using *k.p* Hamiltonian and linear response theory. The spin texture in momentum space reveals a strong spin-momentum locking with different orientations for the valence and conduction bands. Berry curvature distributions around the Dirac points highlight the influence of α parameter demonstrating a topological phase transition in 1T'-MoS₂. For $\alpha < 1$ the spin Hall conductivity is the only non-zero term, corresponding to a quantum spin Hall insulator (QSHI) phase, while for $\alpha > 1$, valley Hall conductivity prevails, indicating a transition to a band insulator (BI). Further analysis explores the spin-valley-resolved Hall conductivity and Chern numbers across varying values of α , V , and Fermi energy, uncovering regions of trivial topological phases (TTP) and the role of the edge modes. The zero total Nernst coefficient across energy ranges suggests strong cancellation between spin and valley contributions, providing insights into the material's potential for thermoelectric applications and spintronic devices.

I. INTRODUCTION

In condensed matter physics, the rise of topological materials has marked a significant shift in research, unveiling quantum phenomena with far-reaching consequences. Among these materials, quantum spin Hall insulators (QSHI) play a crucial role, representing a transformative advancement in our understanding of topologically nontrivial electronic states [1].

The concept of a QSHI was initially introduced by Bernevig et al. [2], signifying a groundbreaking departure from traditional electronic behavior by incorporating topological protection for electronic states. These materials exhibit insulating characteristics in their bulk while supporting stable conducting edge states, paving the way for dissipationless electronic transport and innovative spin-based applications [3–5].

Experimental studies have confirmed the presence of QSHI behavior across various material platforms, including one- and two-dimensional systems as well as engineered heterostructures, broadening the scope of potential applications for these topological electronic states [6–8]. These investigations have shed light on the complex relationship between topological and electronic properties at the core of QSHIs.

Monolayer transition metal dichalcogenides (TMDCs) in the T' structural phase, characterized by the general chemical formula MX₂ with M representing W or Mo and X representing Te, Se, or S, have been theoretically predicted to exhibit properties of a QSHI [9] and attracted attentions [10–17]. 1T'-MoS₂ has emerged as a prominent two-dimensional (2D) material, distinguished by its unique structural and electronic properties. Unlike its more commonly studied counterpart, 2H-MoS₂, which exhibits a stable semiconducting phase, 1T'-MoS₂ adopts distorted octahedral coordination that results in a metallic character and significant potential for various applications in electronics, catalysis, and energy storage. The transition from the 2H to the 1T' phase can be in-

duced through methods such as chemical intercalation or strain engineering, highlighting the material's versatility and tunability [18, 19].

The unique electronic structure of 1T'-MoS₂ is characterized by the presence of helical edge states and strong spin-orbit coupling, which can lead to interesting phenomena such as spin polarization and topological properties [20]. These features make 1T'-MoS₂ a candidate for spintronic applications and quantum computing, where control over electron spin and charge is essential [21]. Furthermore, its high surface area and catalytic activity have positioned it as a promising material for electro-catalytic applications, including hydrogen evolution reactions.

The significance of QSHIs extends beyond theoretical physics, reaching into practical applications in electronics and spintronics. The chiral nature of the edge states in QSHIs presents an exciting opportunity for dissipationless spin transport, which could lead to the development of efficient spin-based logic and memory devices that utilize the spin degrees of freedom of electrons [22–24]. Additionally, the complex interplay between the topological and electronic properties of these materials underlies their potential for enabling topologically protected quantum computation and information processing [25, 26].

Recent theoretical developments have further highlighted the promise of QSHIs in expanding the boundaries of electronic and spin-based functionalities. Proposals for harnessing edge states in QSHIs have opened new pathways for achieving dissipationless spin transport, laying the groundwork for advancements in spin-based information processing and quantum computing [27, 28]. The theoretical models established have not only provided insights into the fundamental behavior of QSHIs but also set the stage for exploring their transformative potential [29–31].

In light of these developments, the experimental realization of the quantum spin Hall effect and the identification of materials with topologically nontrivial electronic

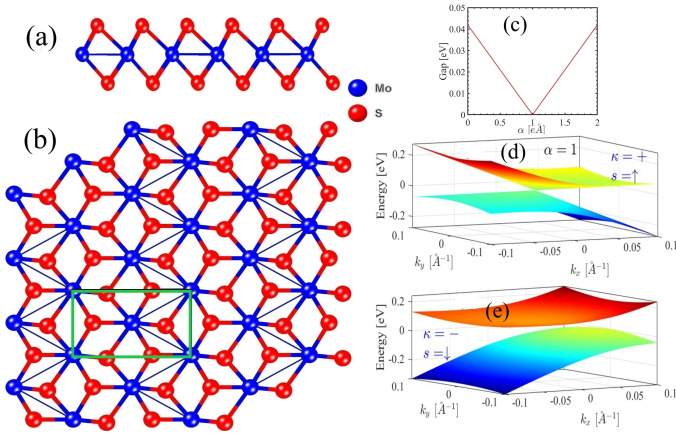


FIG. 1: (a) The side view and (b) the top view of monolayer 1T'-MoS₂, consisting of Mo and S atoms represented in blue and red colors respectively. The unit cell consists of four atoms and is represented by the green rectangle. Panel (c) displays the relationship between the spin-orbit coupling gap and α . Panels (d) and (e) illustrate the 3D band structure for $\alpha = 1$, with $\kappa = +$ and spin $s = \uparrow$, as well as for $\kappa = -$ and spin $s = \downarrow$ respectively.

states have created unique opportunities to exploit their extraordinary properties [32, 33]. The synergy between theory and experiment has propelled the field of topological electronics into an era of unprecedented promise and potential.

Although the topological behavior of 1T'-MoS₂ has been predicted previously, the quantization of the Hall conductivity and consequently the Chern numbers of this material have not been investigated so far. In this study, we prove this topological behavior using $k \cdot p$ Hamiltonian and linear response theory.

This paper begins by exploring the theoretical background in section II to gain insight into the properties of 1T'-MoS₂. Next, theoretical frameworks are applied to calculate these properties in section III, and the results are summarized in section IV.

II. THEORY

Figures 1 (a) and (b) present the top and side views of 1T'-MoS₂, which is composed of two types of atoms: molybdenum (Mo) represented in blue and sulfur (S) shown in red. The unit cell, outlined by a green rectangle, contains four atoms. The low-energy $k \cdot p$ Hamiltonian of monolayer 1T'-MoS₂ in the $x - y$ plane and in presence of a perpendicular electric field E_z and gate voltage V is well addressed before [9, 17, 34]. The Hamiltonian can be written as a summation of the $H_{k \cdot p}$ and external perturbations.

$$H = H_{k \cdot p} + H_{E_z} + V \quad (1)$$

where

$$H_{k \cdot p} = \begin{pmatrix} E_p & 0 & -iv_1 \hbar q_y & v_2 \hbar q_y \\ 0 & E_p & v_2 \hbar q_y & -iv_1 \hbar q_x \\ iv_1 \hbar q_x & v_2 \hbar q_y & E_d & 0 \\ v_2 \hbar q_y & iv_1 \hbar q_x & 0 & E_d \end{pmatrix} \quad (2)$$

and

$$H_{E_z} = \alpha \Delta_{so} \begin{pmatrix} 0 & 0 & 1 & 0 \\ 0 & 0 & 0 & 1 \\ 1 & 0 & 0 & 0 \\ 0 & 1 & 0 & 0 \end{pmatrix} \quad (3)$$

Here, V is a 4×4 diagonal matrix, and $\Delta_{so} = 41.9 \text{ meV}$ represents the fundamental spin-orbit coupling gap at the Dirac points $(0, \kappa\Lambda)$. The parameter α is defined as $|E_z/E_c|$, where E_z is the perpendicular electric field and $E_c = 1.42 \text{ V/nm}^{-1}$ is the critical electric field required for a topological phase transition. The on-site energies for the p and d orbitals are given by the $E_p = \delta_p + \frac{\hbar^2 q_x^2}{2m_p^x} + \frac{\hbar^2 q_y^2}{2m_p^y}$ and $E_d = \delta_d + \frac{\hbar^2 q_x^2}{2m_d^x} + \frac{\hbar^2 q_y^2}{2m_d^y}$ respectively, where $q_{x,y}$ is the electron momentum. The parameters are defined as follows: $\delta_p = 0.46 \text{ eV}$, $\delta_d = -0.20 \text{ eV}$, $m_p^x = -0.50 m_0$, $m_p^y = -0.16 m_0$, $m_d^x = 2.48 m_0$, $m_d^y = 0.37 m_0$, and m_0 is the free electron mass, $\nu_1 = 3.87 \times 10^5 \text{ m/s}$ and $\nu_2 = 0.46 \times 10^5 \text{ m/s}$ are the Fermi velocities along the x and y directions respectively.

Using a unitary transformation the Hamiltonian reads as

$$H_{\kappa,s}(k) = \hbar k_x \nu_1 \sigma_y - \hbar k_y (s \nu_2 \sigma_x + \kappa \nu_- \sigma_0 + \kappa \nu_+ \sigma_z) + \Delta_{so} (\alpha - s \kappa) \sigma_x + V \sigma_0 \quad (4)$$

Where $s = \pm$ is related to the spin up and down respectively, and $\kappa = \pm$ represents valley indexes (K and K'). The tilting velocities are $\nu_- = \frac{\hbar q_0}{2} (-\frac{1}{m_p^x} - \frac{1}{m_d^y}) = 2.84 \times 10^5 \text{ m/s}$ and $\nu_+ = \frac{\hbar q_0}{2} (-\frac{1}{m_p^y} + \frac{1}{m_d^x}) = 7.18 \times 10^5 \text{ m/s}$.

After diagonalization of the Hamiltonian, the eigen energies are

$$\varepsilon_{\kappa,s}^{\pm}(k_x, k_y) = -\hbar k_y \kappa \nu_- + V \pm \sqrt{[\zeta_{\kappa,s}(k_y)]^2 + [\Lambda(k_y)]^2 - [\eta(k_x)]^2} \quad (5)$$

and corresponding eigenstates are

$$\psi_{\kappa,s}^{\pm}(k_x, k_y) = \begin{pmatrix} \mp \eta(k_x) \mp \zeta_{\kappa,s}(k_y) \\ \pm \Lambda_{\kappa}(k_y) + \sqrt{[\zeta_{\kappa,s}(k_y)]^2 + [\Lambda(k_y)]^2 - [\eta(k_x)]^2} \\ 1 \end{pmatrix} \quad (6)$$

where

$$\zeta_{\kappa,s}(k_y) = \hbar k_y s \nu_2 - \Delta_{so} (\alpha - s \kappa) \quad (7)$$

$$\Lambda_{\kappa}(k_y) = \hbar k_y \kappa \nu_+ \quad (8)$$

$$\eta(k_x) = i\hbar k_x \nu_1 \quad (9)$$

The 3D band structure of 1T'-MoS₂ is depicted in Figs. 1 (d) and (e) under the influence of an electric field ($\alpha \neq 0$). When $\alpha = 1$, $\kappa = +$, and $s = \uparrow$, the spin-orbit gap is closed (see Fig. 1 (c)). Conversely, for $\kappa = -$ and $s = \downarrow$, a small gap of approximately 0.04eV is observed. As we will demonstrate later, this critical amount of the α is a key factor in the topological phase transition.

Pseudo-spin texture in 1T'-MoS₂ emerges from its unique electronic structure, particularly due to the presence of two distinct valleys in the Brillouin zone, often referred to as the K and K' valleys. These valleys can be treated as pseudo-spin states, where electrons in the K valley are analogous to spin-up and those in the K' valley to spin-down.

The two components of the pseudo-spin textures can be calculated by $S_x^\pm = \langle \psi_{\kappa,s}^\pm | \sigma_x | \psi_{\kappa,s}^\pm \rangle$ and $S_y^\pm = \langle \psi_{\kappa,s}^\pm | \sigma_y | \psi_{\kappa,s}^\pm \rangle$, where σ_x and σ_y are the Pauli matrices and \pm , stems for the pseudo-spin texture in the conduction and valence band respectively. After some algebra we have

$$S_x^\pm = \mp \frac{2\zeta_{\kappa,s}(k_y)}{\pm\Lambda_\kappa(k_y) + \sqrt{[\zeta_{\kappa,s}(k_y)]^2 + [\Lambda(k_y)]^2} - [\eta(k_x)]^2} \quad (10)$$

and

$$S_y^\pm = \pm \frac{2\hbar k_x \nu_1}{\pm\Lambda_\kappa(k_y) + \sqrt{[\zeta_{\kappa,s}(k_y)]^2 + [\Lambda(k_y)]^2} - [\eta(k_x)]^2} \quad (11)$$

The azimuthal angle of the pseudo-spin can be expressed as

$$\tan(\theta_s) = \frac{S_y}{S_x} = -\frac{\hbar k_x \nu_1}{\hbar k_y \nu_2 - \Delta_{so}(\alpha - s\kappa)} \quad (12)$$

We calculate optical Hall conductivity using the Kubo formula and Berry curvatures. The Kubo formula for Hall conductivity is given by [35–37]

$$\sigma_{\kappa,s} = \frac{e}{h} \int f_{\kappa,s}^n(\vec{k}) \Omega_{\kappa,s}^n(\vec{k}) d^2k \quad (13)$$

Where the Berry curvature and direction-dependent velocities operators are defined as

$$\Omega_{\kappa,s}^n(\vec{k}) = -2\text{Im} \sum_{n' \neq n} \frac{\beta_{\kappa,s}^{n,n',x}(\vec{k}) \beta_{\kappa,s}^{n',n,y}(\vec{k})}{(\varepsilon_{\vec{k},\kappa,s}^n - \varepsilon_{\vec{k},\kappa,s}^{n'})^2}. \quad (14)$$

$$\beta_{\kappa,s}^{n,n',x}(\vec{k}) = \langle \vec{k}; n, \kappa, s | j_x | \vec{k}; n', \kappa, s \rangle \quad (15)$$

$$\beta_{\kappa,s}^{n',n,y}(\vec{k}) = \langle \vec{k}; n', \kappa, s | j_y | \vec{k}; n, \kappa, s \rangle \quad (16)$$

The expression $f_{\kappa,s}^n(\vec{k}) = [1 + \exp(\varepsilon_{\kappa,s}^n - E_F)/k_B T]^{-1}$ represents the Fermi-Dirac distribution function for the n th band, where E_F denotes the Fermi energy. The index $n = \pm$ indicates the conduction and valence bands, respectively. Also, the quantities $j_x = e\partial H_{\kappa,s}(\vec{k})/\partial k_x$, and $j_y = e\partial H_{\kappa,s}(\vec{k})/\partial k_y$ describe the direction-dependent velocities along the x and y axes.

The spin-valley-resolved Hall conductivity is expressed as $\sigma_{\kappa,s} = e^2/hC_{\kappa,s}$, where $C_{\kappa,s}$ represents the spin-valley-resolved Chern number

$$C_{\kappa,s} = \frac{1}{2\pi} \int f_{\kappa,s} \Omega_{\kappa,s}^n(\vec{k}) d^2k \quad (17)$$

The spin and valley Chern numbers are given by $C_s = (C_\uparrow - C_\downarrow)/2$ and $C_v = (C_+ - C_-)/2$, respectively, in which $C_{\uparrow(\downarrow)} = \sum_\kappa C_{\kappa,\uparrow(\downarrow)}$ and $C_{+(-)} = \sum_s C_{+(-),s}$.

Having Berry curvatures we can calculate spin-valley Nernst coefficient as [38, 39]

$$\Gamma_{\kappa,s}^n = \frac{ek_B}{2\pi\hbar} \sum_n \int \Omega_{\kappa,s}^n(\vec{k}) S_{\kappa,s}^n(\vec{k}) dk^2 \quad (18)$$

where the entropy density is given by $S_{\kappa,s}^n(\vec{k}) = -f_n(\vec{k}) \ln f_n(\vec{k}) - [1 - f_n(\vec{k})] \ln [1 - f_n(\vec{k})]$. The TNC can be calculated by summing over all spin-valley resolved NCs ($\Gamma_\uparrow + \Gamma_\downarrow + \Gamma_+ + \Gamma_-$) and the spin SNC and VNC are defined as $\Gamma_s = \Gamma_\uparrow - \Gamma_\downarrow$ and $\Gamma_v = \Gamma_+ - \Gamma_-$ respectively.

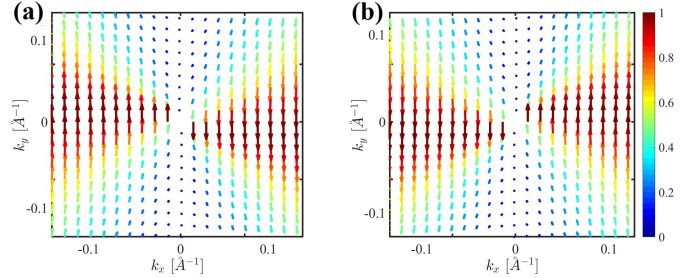


FIG. 2: Pseudo-spin texture in the momentum space for (a) conduction band and (b) valence band.

III. RESULTS AND DISCUSSION

Figures 2 (a) and (b) illustrate the spin texture in momentum space for the conduction and valence bands respectively. The color of the arrows shows the magnitude of the spin $s = \sqrt{s_x^2 + s_y^2}$ varies from 0 (blue) to 1 (red). The tangential alignment of spins with momentum indicates spin-momentum locking, a signature of systems with topological properties. The absence of spin at the

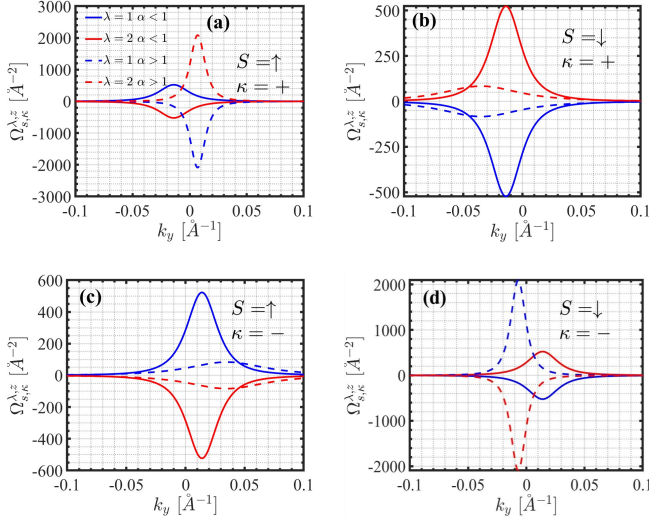


FIG. 3: Conduction and valence Berry curvature around the Dirac points for $\alpha = 0$ and $\alpha = 1.5$ in (a) $\kappa = +$, $s = \uparrow$, (b) $\kappa = +$, $s = \downarrow$, (c) $\kappa = -$, $s = \uparrow$, and (d) $\kappa = -$, $s = \downarrow$. $\lambda = 1$ and $\lambda = 2$ refer to the valence and conduction bands respectively.

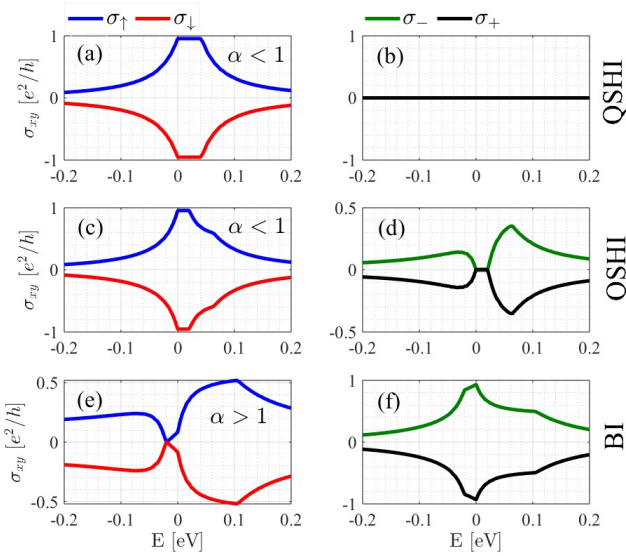


FIG. 4: Spin and valley Hall conductivities with respect to the Fermi energy at $T = 0$ K for $\alpha < 1$ and $\alpha > 1$.

$\vec{k} = (0, 0)$ suggests a Dirac-like point, where the energy bands cross, forming a spin-degenerate state. This is a hallmark of Dirac systems. The spin texture exhibits slightly elongated features along the k_y direction, which implies anisotropy in the band structure. Indeed, The spin configuration displays mirror symmetry with respect to both $k_x = 0$ and $k_y = 0$, indicating the presence of the time-reversal symmetry.

The behavior of Berry curvatures around the Dirac points for various values of α and different bands is depicted in Figs. 3 (a-d). Here, $\lambda = 1$ and $\lambda = 2$ correspond to the valence and conduction bands respectively. In all

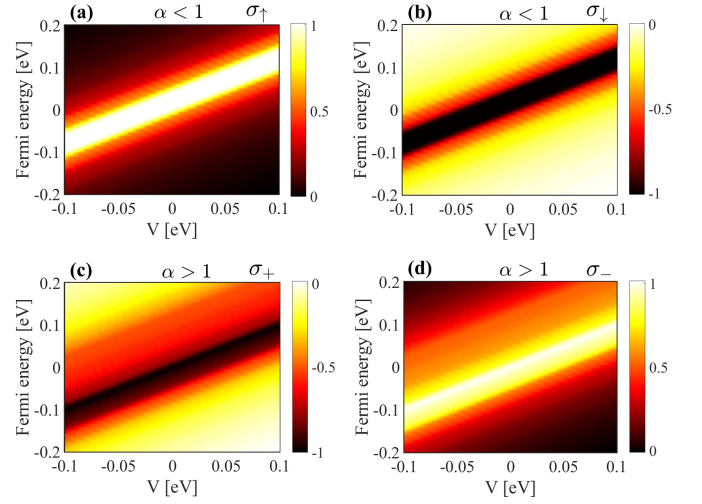


FIG. 5: The color density of the spin-valley-resolved Hall conductivity versus V and the Fermi energy. Panel (a) and (b) show spin-resolved Hall conductivity for spin-up and spin-down respectively while $\alpha < 1$, (c) and (d) is valley-resolved Hall conductivity for $\kappa = \pm$ respectively for $\alpha > 1$.

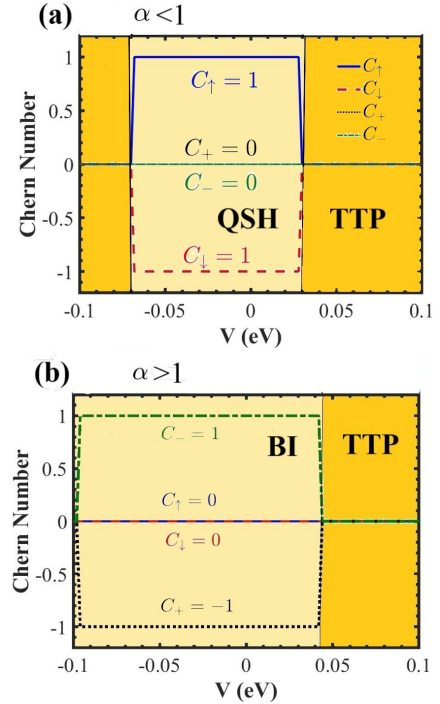


FIG. 6: The Chern number versus V in the presence of the electric field for (a) $\alpha < 1$ and (b) α . The colored areas show the topological phase of the system.

scenarios, $\Omega_{\kappa,s}^n(\vec{k})$ is predominantly localized near the K and K' valleys. Large peaks near the Dirac points indicate strong topological effects at these points, which could result in phenomena like anomalous velocity, orbital magnetization, or spin Hall effects. For $s = \uparrow$ and $\alpha < 1$ (with $\kappa = \pm$), the sign of the conduction band

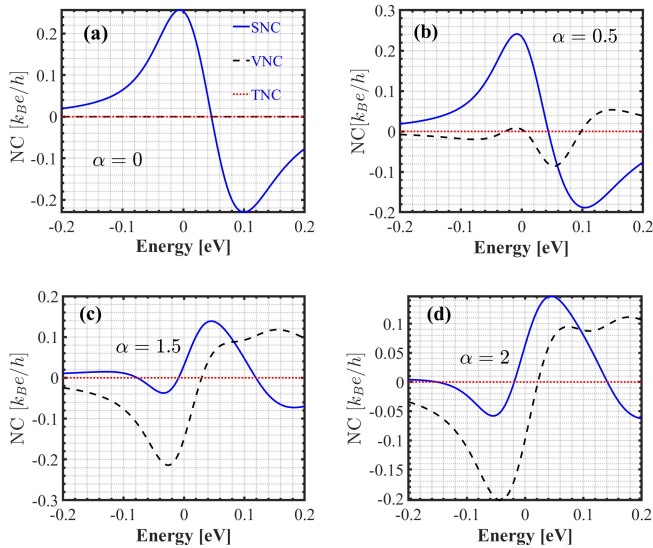


FIG. 7: The spin (SNC), valley (VNC), and total Nernst coefficient (TNC) versus the Fermi energy at $T = 300$ K for different values of α . The blue, black, and red curves show SNC, VNC and TNC respectively.

Berry curvature is positive (and negative for the valence band). However, for $\alpha > 1$, the signs of the Berry curvatures are reversed. This alteration in the sign of the Berry curvature indicates a topological phase transition in 1T'-MoS2. The opposite signs for the conduction and valence bands suggest a contribution to opposite topological currents from electrons in these bands, which could cancel or add under specific conditions. In contrast, for $s = \downarrow$, the signs of the Berry curvatures for both the conduction and valence bands are opposite to those observed for $s = \uparrow$. The opposing signs of the Berry curvature for the conduction and valence bands suggest that the material could host a nontrivial topology, potentially enabling edge states or chiral transport. This feature is key in materials with nonzero Chern numbers or topological invariants.

The spin-valley-resolved Hall conductivity is illustrated in Fig. 4 for various values of α . When $\alpha < 1$, the spin-resolved Hall conductivity reaches maximum values of ± 1 for spin-up and spin-down, respectively, while the valley-resolved Hall conductivity is zero (see Fig. 4 (a) and (b)) and consequently $C_v = 0$ and $C_s = 1$ which shows QSHI phase. In this scenario, the energy range where the Hall conductivity remains constant indicates a spin-orbit coupling gap of about $0.04eV$. As shown in Fig. 4 (b) and Fig. 4 (c), when we increase α to higher amounts (still $\alpha < 1$), the valley-resolved Hall conductivity becomes non-zero; however, the spin-resolved Hall conductivity continues to dominate. This increase in α reduces the spin-orbit coupling gap, which is consistent with the observations in Fig. 1 (c). The Hall conductivity for $\alpha > 1$ is different in comparison with $\alpha < 1$. In this case, the valley-resolved Hall conductivity is non-zero and is the dominant term. The maximum amounts of the

Hall conductivity are ± 1 which are related to the σ_{\mp} respectively and we have $C_s = 0$ and $C_v = 1$. This change in the Hall conductivity for $\alpha > 1$ is an evidence for the topological phase transition between QSHI-to-BI which is consistent with previous study [40].

To cover the entire range of V and Fermi energy, we plotted the color density of the spin-valley-resolved Hall conductivity as a function of V and Fermi energy for both $\alpha < 1$ and $\alpha > 1$ (see Fig. 5). For $\alpha < 1$ ($\alpha > 1$), the valley-resolved Hall conductivity (spin-resolved Hall conductivity) is zero, so we omitted these zero terms from our plots. A prominent diagonal bright region (white-yellow) extends linearly through the origin (see Fig. 5 (a)). The slope of this bright region suggests a direct relationship between V and E_F , meaning changes in the gate voltage correspond to shifts in the Fermi energy. Away from the central bright stripe, the conductivity rapidly decreases, as evidenced by the transition to darker shades (red to black). This indicates that the Hall response is sharply localized in the $V - E_F$ space. This region indicates a peak in the Hall conductivity ($\sigma_{\uparrow} = 1$) that aligns with specific combinations of V and E_F . As E_F moves away from the band edges, the Hall conductivity decreases. This behavior is consistent with the vanishing Berry curvature in regions of k -space far from band crossings, where the bands are less topologically active. As V increases, this maximum shifts towards higher Fermi energies, and it is clear that the width of the Fermi energy remains constant, indicating that the topological gap is independent of the V amount. A similar condition applies to σ_{\downarrow} for $\alpha < 1$ across different values of V , as shown in Fig. 5 (b). The maximum value of σ_{\downarrow} is -1 , which is located at the same position as that of σ_{\uparrow} . Since for $\alpha < 1$, the valley-resolved Hall conductivity is zero, we only plotted it for $\alpha > 1$ (see Figs. 5 (c) and (d)). In this scenario, the maximum value of the Valley Hall conductivity is $\sigma_{+} = -1$ which is localized at certain combinations of V and E_F . As V increases (decreases), the Fermi energy interval shifts to higher (lower) energies. The valley Hall conductivity for σ_{-} reaches a maximum value of $+1$ and exhibits behavior similar to that of σ_{+} (Fig 5 (d)).

We plotted the Chern number as a function of V for varying values of α at $E_F = 0$ and $T = 0$. Figure. 6 (a), shows the Chern numbers for $\alpha < 1$. The valley-resolved Hall conductivity remains zero across all V values. However, in the interval $-0.07 \leq V \leq 0.03$, we find a non-zero spin-resolved Hall conductivity with $C_{\uparrow} = 1$, $C_{\downarrow} = -1$ and $C_s = 1$, indicating the presence of a QSHI phase. In this case, both spins have the helical edge mode. For values of $V \leq -0.07$ and $V \geq 0.03$, the Hall conductivity vanishes, resulting in a trivial topological phase (TTP). However, when $\alpha > 1$, a topological phase transition occurs from QSHI-to-BI, characterized by $C_{\uparrow, \downarrow} = 0$, $C_{+} = -1$, and $C_{-} = 1$ (see Fig. 6 (b)). In this case, $C_s = 0$ and $C_v = 1$, which leads to the absence of the spin edge modes. Notably, for $\alpha > 1$ there is a wider range of V values where the Hall conductivity is non-

zero (see Fig. 6 (c)). It is necessary to mention that when the Fermi energy falls within a band ($\alpha = 1$), the Chern number is not defined, however, the Kubo formula can still provide the Hall conductivity.

We calculated the spin Nernst (SNC), valley Nernst (VNC), and total Nernst coefficients (TNC) as functions of the Fermi energy at room temperature for various values of α . As shown in Fig. 7. For all values of α , the TNC remains zero across the energy range, indicating a strong cancellation between the spin and valley contributions. When $\alpha = 0$ (see Fig. 7 (a)), the only non-zero term is SNC. The SNC exhibits a clear asymmetry around zero energy, with a significant negative (positive) peak at positive (negative) energies. This behavior suggests that the spin-related transport properties vary with the energy landscape. As an electric field is applied, the VNC begins to increase; however, SNC still dominates (Fig. 7 (b)). When α is increased to 1.5 and 2 (see Figs. 7 (c) and (d)), the VNC has a pronounced negative peak at slightly negative energies and transitions to a less negative or slightly positive regime at higher energies. This indicates a significant valley-dependent response that is similar in sign to the spin contribution in certain regions. The spin Nernst effect is dominant in the positive energy range, where it exhibits a positive peak. On the other hand, the valley Nernst effect is dominant in the negative energy range, contributing to a negative peak. The zero total Nernst coefficient suggests that, while the individual contributions are large, their combined transport

properties result in minimal net transverse voltage under a thermal gradient.

IV. CONCLUSIONS

In conclusion, this study highlights the rich interplay between spin, valley, and topological properties in systems exhibiting Rashba spin-splitting and strong spin-orbit coupling. The analysis of spin textures reveals hallmark features such as spin-momentum locking, anisotropy in the band structure, and the presence of Dirac points, underscoring their potential for spintronic applications. The Berry curvature and Hall conductivity analyses demonstrate that the system undergoes a topological phase transition from a QSHI-to-BI phase as the parameter α is varied, with distinct spin-resolved and valley-resolved contributions to the Hall conductivity. Furthermore, the behavior of the spin and valley Nernst coefficients reveals nuanced energy-dependent transport phenomena, where significant contributions from spin and valley effects largely cancel each other, resulting in a zero total Nernst coefficient.

DATA AVAILABILITY

The data that support the findings of this study are available from the corresponding author upon reasonable request.

-
- [1] M. Z. Hasan and C. L. Kane, Colloquium: Topological insulators, *Rev. Mod. Phys.* **82**, 3045 (2010).
 - [2] B. A. Bernevig and S.-C. Zhang, Quantum spin hall effect, *Phys. Rev. Lett.* **96**, 106802 (2006).
 - [3] X.-L. Qi and S.-C. Zhang, Topological insulators and superconductors, *Rev. Mod. Phys.* **83**, 1057 (2011).
 - [4] D. Hsieh, Y. Xia, D. Qian, L. Wray, J. H. Dil, F. Meier, J. Osterwalder, L. Patthey, J. G. Checkelsky, N. P. Ong, A. V. Fedorov, H. Lin, A. Bansil, D. Grauer, Y. S. Hor, R. J. Cava, and M. Z. Hasan, A tunable topological insulator in the spin helical dirac transport regime, *Nature* **460**, 1101 (2009).
 - [5] D. Bercioux and P. Lucignano, Quantum transport in rashba spin-orbit materials: a review, *Reports on Progress in Physics* **78**, 106001 (2015).
 - [6] M. König, S. Wiedmann, C. Brüne, A. Roth, H. Buhmann, L. W. Molenkamp, X.-L. Qi, and S.-C. Zhang, Quantum spin hall insulator state in hgte quantum wells, *Science* **318**, 766 (2007), <https://www.science.org/doi/pdf/10.1126/science.1148047>.
 - [7] B. Yan and S.-C. Zhang, Topological materials, *Reports on Progress in Physics* **75**, 096501 (2012).
 - [8] C. Brune, A. Roth, H. Buhmann, E. M. Hankiewicz, L. W. Molenkamp, J. Maciejko, X.-L. Qi, and S.-C. Zhang, Spin polarization of the quantum spin hall edge states, *Nature Physics* **8**, 485 (2012).
 - [9] X. Qian, J. Liu, L. Fu, and J. Li, Quantum spin hall effect in two-dimensional transition metal dichalcogenides, *Science* **346**, 1344 (2014), <https://www.science.org/doi/pdf/10.1126/science.1256815>.
 - [10] D. Xiao, G.-B. Liu, W. Feng, X. Xu, and W. Yao, Coupled spin and valley physics in monolayers of mos₂ and other group-vi dichalcogenides, *Phys. Rev. Lett.* **108**, 196802 (2012).
 - [11] Q. H. Wang, K. Kalantar-Zadeh, A. Kis, J. N. Coleman, and M. S. Strano, Electronics and optoelectronics of two-dimensional transition metal dichalcogenides, *Nature Nanotechnology* **7**, 699 (2012).
 - [12] X. Xu, W. Yao, D. Xiao, and T. F. Heinz, Spin and pseudospins in layered transition metal dichalcogenides, *Nature Physics* **10**, 343 (2014).
 - [13] S. Manzeli, D. Ovchinnikov, D. Pasquier, O. V. Yazyev, and A. Kis, 2d transition metal dichalcogenides, *Nature Reviews Materials* **2**, 17033 (2017).
 - [14] S. Wu, V. Fatemi, Q. D. Gibson, K. Watanabe, T. Taniguchi, R. J. Cava, and P. Jarillo-Herrero, Observation of the quantum spin hall effect up to 100 kelvin in a monolayer crystal, *Science* **359**, 76 (2018), <https://www.science.org/doi/pdf/10.1126/science.aan6003>.
 - [15] Y. Ominato, J. Fujimoto, and M. Matsuo, Valley-dependent spin transport in monolayer transition-metal dichalcogenides, *Phys. Rev. Lett.* **124**, 166803 (2020).

- [16] S. Tang, C. Zhang, D. Wong, Z. Pedramrazi, H.-Z. Tsai, C. Jia, B. Moritz, M. Claassen, H. Ryu, S. Kahn, J. Jiang, H. Yan, M. Hashimoto, D. Lu, R. G. Moore, C.-C. Hwang, C. Hwang, Z. Hussain, Y. Chen, M. M. Ugeda, Z. Liu, X. Xie, T. P. Devereaux, M. F. Crommie, S.-K. Mo, and Z.-X. Shen, Quantum spin hall state in monolayer $1t'$ -wte₂, *Nature Physics* **13**, 683 (2017).
- [17] B. Das, D. Sen, and S. Mahapatra, Tuneable quantum spin hall states in confined $1t'$ transition metal dichalcogenides, *Scientific Reports* **10**, 6670 (2020).
- [18] D. Wang, X. Zhang, S. Bao, Z. Zhang, H. Fei, and Z. Wu, Phase engineering of a multiphase $1t'/2h$ mos₂ catalyst for highly efficient hydrogen evolution, *J. Mater. Chem. A* **5**, 2681 (2017).
- [19] A. Chakraborty, R. González Hernández, L. Šmejkal, and J. Sinova, Strain-induced phase transition from antiferromagnet to altermagnet, *Phys. Rev. B* **109**, 144421 (2024).
- [20] R. Luo, W. W. Xu, Y. Zhang, Z. Wang, X. Wang, Y. Gao, P. Liu, and M. Chen, Van der waals interfacial reconstruction in monolayer transition-metal dichalcogenides and gold heterojunctions, *Nature Communications* **11**, 1011 (2020).
- [21] Y. Niu, P. Wang, and M. Zhang, Tuning the spin polarization in monolayer mos₂ through (y,yb) co-doping, *New J. Chem.* **44**, 20316 (2020).
- [22] D. Pesin and A. H. MacDonald, Spintronics and pseudospintronics in graphene and topological insulators, *Nature Materials* **11**, 409 (2012).
- [23] R. Jansen, Silicon spintronics, *Nature Materials* **11**, 400 (2012).
- [24] A. Manchon, H. C. Koo, J. Nitta, S. M. Frolov, and R. A. Duine, New perspectives for rashba spin-orbit coupling, *Nature Materials* **14**, 871 (2015).
- [25] A. Kitaev, Fault-tolerant quantum computation by anyons, *Annals of Physics* **303**, 2 (2003).
- [26] C. Nayak, S. H. Simon, A. Stern, M. Freedman, and S. Das Sarma, Non-abelian anyons and topological quantum computation, *Rev. Mod. Phys.* **80**, 1083 (2008).
- [27] S. M. Young and C. L. Kane, Dirac semimetals in two dimensions, *Phys. Rev. Lett.* **115**, 126803 (2015).
- [28] J. Maciejko, C. Liu, Y. Oreg, X.-L. Qi, C. Wu, and S.-C. Zhang, Kondo effect in the helical edge liquid of the quantum spin hall state, *Phys. Rev. Lett.* **102**, 256803 (2009).
- [29] L. Fu, Topological crystalline insulators, *Phys. Rev. Lett.* **106**, 106802 (2011).
- [30] H. Zhang, C.-X. Liu, X.-L. Qi, X. Dai, Z. Fang, and S.-C. Zhang, Topological insulators in bi_2se_3 , bi_2te_3 and sb_2te_3 with a single dirac cone on the surface, *Nature Physics* **5**, 438 (2009).
- [31] M. Mortezaei Nobahari and C. Autieri, Spin-hall conductivity and optical characteristics of noncentrosymmetric quantum spin hall insulators: the case of pbbii, *Scientific Reports* **14**, 27041 (2024).
- [32] S.-Y. Xu, C. Liu, N. Alidoust, M. Neupane, D. Qian, I. Belopolski, J. D. Denlinger, Y. J. Wang, H. Lin, L. A. Wray, G. Landolt, B. Slomski, J. H. Dil, A. Marcinkova, E. Morosan, Q. Gibson, R. Sankar, F. C. Chou, R. J. Cava, A. Bansil, and M. Z. Hasan, Observation of a topological crystalline insulator phase and topological phase transition in pb₁, *Nature Communications* **3**, 1192 (2012).
- [33] X. Kou, S.-T. Guo, Y. Fan, L. Pan, M. Lang, Y. Jiang, Q. Shao, T. Nie, K. Murata, J. Tang, Y. Wang, L. He, T.-K. Lee, W.-L. Lee, and K. L. Wang, Scale-invariant quantum anomalous hall effect in magnetic topological insulators beyond the two-dimensional limit, *Phys. Rev. Lett.* **113**, 137201 (2014).
- [34] D. Wang, A. Hu, J.-P. Lv, and G. Jin, Electric field modulated valley- and spin-dependent electron retroreflection and klein tunneling in a tilted $n-p-n$ junction of monolayer $1T'$ -mos₂, *Phys. Rev. B* **107**, 035301 (2023).
- [35] M. Mortezaei Nobahari, Electro-optical properties of strained monolayer boron phosphide, *Scientific Reports* **13**, 9849 (2023).
- [36] D. Xiao, M.-C. Chang, and Q. Niu, Berry phase effects on electronic properties, *Rev. Mod. Phys.* **82**, 1959 (2010).
- [37] Y. Hajati, M. Alipourzadeh, and J. Berakdar, Magneto-electric tuning of spin, valley, and layer-resolved anomalous nernst effect in transition-metal dichalcogenides bilayers, *Journal of Physics: Condensed Matter* **35**, 285602 (2023).
- [38] X.-Q. Yu, Z.-G. Zhu, G. Su, and A.-P. Jauho, Thermally driven pure spin and valley currents via the anomalous nernst effect in monolayer group-vi dichalcogenides, *Phys. Rev. Lett.* **115**, 246601 (2015).
- [39] Y. Xu, X. Zhou, and G. Jin, Detecting topological phases in silicene by anomalous nernst effect, *Applied Physics Letters* **108**, 203104 (2016), https://pubs.aip.org/aip/apl/article-pdf/doi/10.1063/1.4950854/13607510/203104_1_online.pdf.
- [40] C.-Y. Tan, C.-X. Yan, Y.-H. Zhao, H. Guo, and H.-R. Chang, Anisotropic longitudinal optical conductivities of tilted dirac bands in $1T'$ -Mos₂, *Phys. Rev. B* **103**, 125425 (2021).